Supplementary Information

Atomic-scale Mechanism of Alloy Anodes Mitigating Polysulfide-induced Degradation in Lithium-Sulfur Batteries

Il-Seok Jeong[1], Hidemi Kato[2], Byungki Ryu[3,4], Eun-Ae Choi[1,2,5*] and Seung Zeon Han[1,2,5*]

[1]Extreme Materials Research Institute, Korea Institute of Materials Science (KIMS), Changwon 51508, Republic of Korea
[2]Institute for Materials Research (IMR), Tohoku University, Sendai 980-8577, Japan
[3]Energy Conversion Research Center, Electrical Materials Research Division, Korea Electrotechnology Research Institute (KERI), Changwon 51543, Republic of Korea.
[4]Electric Energy and Materials Engineering, School of KERI, University of Science and Technology, Changwon 51543, Republic of Korea
[5]Advanced Materials Engineering, School of KIMS, University of Science and Technology, Changwon 51508, Republic of Korea

[*]To whom correspondence should be addressed: szhan@kims.re.kr and eunae.choi@kims.re.kr

This Supplementary Information provides comprehensive supporting data and detailed analyses that complement the main findings presented in the manuscript. The supplementary materials are organized to offer deeper insights into the atomic-scale mechanisms underlying how lithium alloy anodes suppress polysulfide-induced degradation in lithium-sulfur batteries.

Supplementary Table 1 establishes the fundamental rationale for selecting Mg, Al, and Zn as alloying elements, presenting both the fundamental properties of individual elements and the electrochemical characteristics of Li-M alloy systems.

Supplementary Table 1. Comprehensive property database for Li-ion battery anode materials: (a) Fundamental elemental properties from SI references [1-5]; (b) Electrochemical properties of Li-M alloy systems compiled from main manuscript references [26,27,33,35-40].

(a) Fundamental properties of elements

Property	Li	Mg	Al	Zn
Crystal structure	BCC[1]	HCP[1]	FCC[1]	HCP[1]
Atomic radius (Å)	1.52[1]	1.60[1]	1.43[1]	1.39[1]
Ionic radius (Å)	0.76[2]	0.72[2]	0.53[2]	0.75[2]
Density (g cm^{-3})	0.53[3]	1.3[3]	2.7[3]	7.14[3]
Young's modulus (GPa)	4.9[1]	45[1]	70[1]	108[1]
Melting temperature (K)	454[1]	923[1]	933[1]	693[1]
Voltage (V, vs. Li^+/Li)	0[3]	0.0325[3]	0.380[3]	0.157[3]
Theoretical specific capacity ($mAhg^{-1}$)	3860[4]	2233[5]	2978[5]	825[5]
Theoretical volume capacity ($mAh\ cm^{-3}$)	2061[2]	3833[2]	8050[2]	5854[2]

(b) Electrochemical properties of Li-M (M = Mg, Al, Zn) alloy systems

Property	Li	Li-Mg	Li-Al	Li-Zn
Alloy concentration (x)	-	0.05[39],0.06[38],0.10[39], 0.11[40],0.20[39],0.30[40]	0.06[35]	0.50[27]
Phase	BCC[26]	BCC[38-40]	Li_9Al_4[35],LiAl[36,37]	LiZn[26,27,33]
Specific Capacity ($mAhg^{-1}$)	3860[26]	1930[40], 2950[38],	993[37], 3215[35]	355[26]
Average potential (V vs. Li/Li^+)	0.0[26]	0.2–0.4[40]	0.34[37], 0.35–0.4[26]	0.18[26]
Volume change (%)	~100 (Infinite)[26]	80[40], 100[27]	95[37],96[26],97[27]	71[27]
Li diffusion coefficient ($cm^2 s^{-1}$)	5.69×10^{-11} [26]	10^{-7} [26]	6×10^{-10} [26]	4.7×10^{-8} [27]

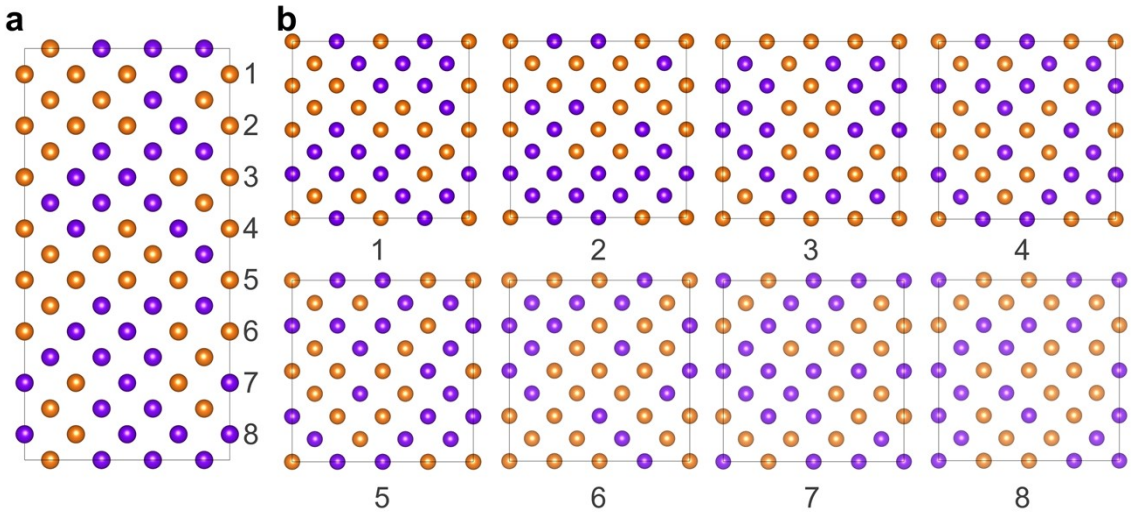

Supplementary Figure 1. Atomic configurations of $Li_{0.5}Mg_{0.5}$ alloy structure in a 4x4x8 supercell: (a) side view showing eight atomic layers; (b) top views of individual layers showing Li (purple) and Mg (orange) atom distribution.

The structural foundation of our computational approach is illustrated in Supplementary Figure 1, which shows the BCC supercell containing 256 atoms constructed using the SQS method for molecular dynamics simulations. Each of the eight layers exhibits distinct morphology, providing the basis for statistical sampling across diverse surface configurations.

Supplementary Figure 2 presents the DFT-optimized structures across different alloy compositions, revealing composition-dependent lattice distortions as alloying element concentrations increase from x = 0.05 to 0.50. The structural evolution shows distinct behavior patterns among the three alloy systems: Mg atoms, with similar atomic radii to Li, maintain relatively stable BCC lattice configurations across all compositions, while Al and Zn atoms, having smaller atomic radii, induce progressively pronounced structural deviations from ideal BCC positions at higher concentrations. These DFT-optimized configurations serve as the initial structures for subsequent MD simulations.

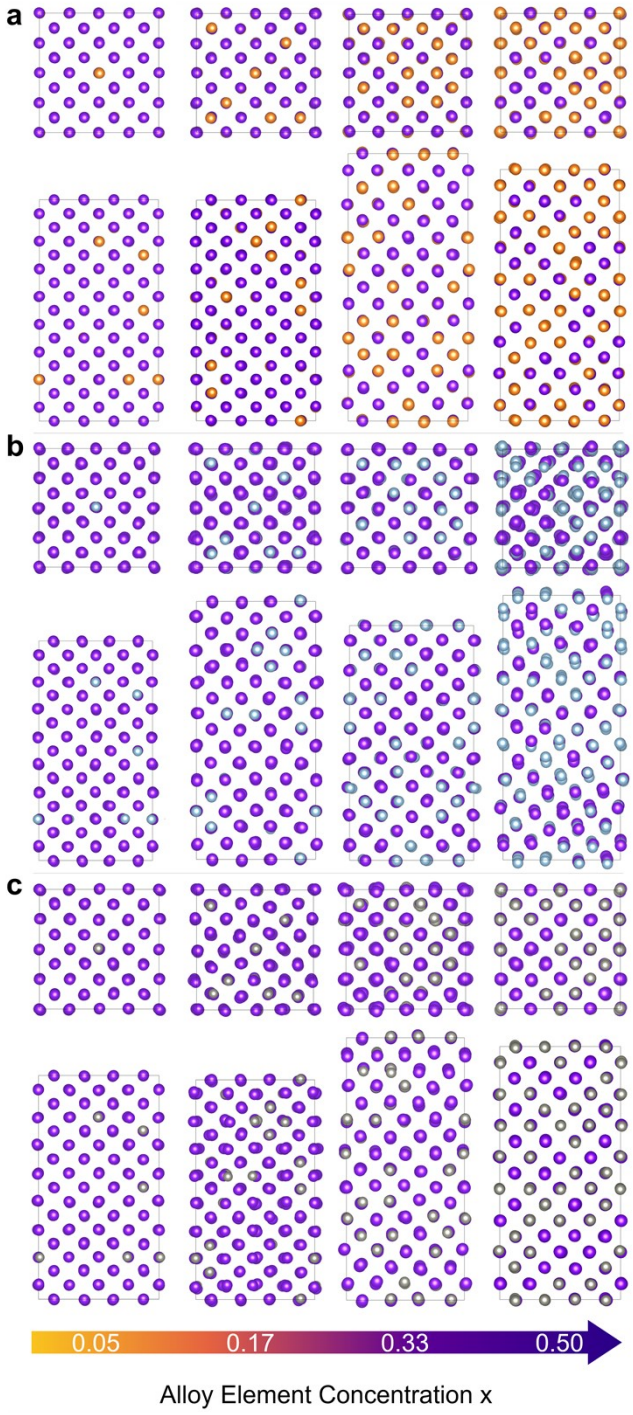

Supplementary Figure 2. Optimized $Li_{1-x}M_x$ alloy anode structures: (a) Li-Mg, (b) Li-Al, and (c) Li-Zn systems shown in top view (upper row) and side view (lower row) with compositions x = 0.05, 0.17, 0.33, and 0.50.

1

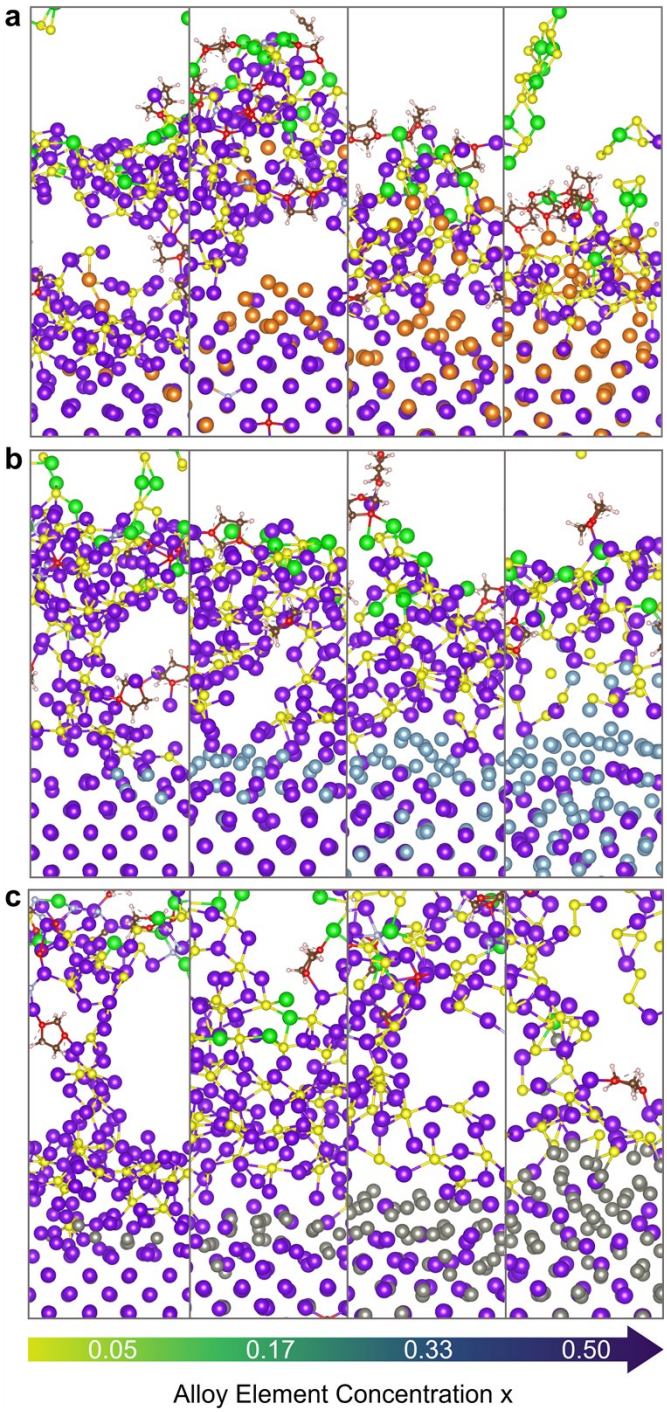

Supplementary Figure 3. Surface corrosion evolution of Li-M alloys with varying compositions over 20 ps: (a) $Li_{1-x}Mg_x$, (b) $Li_{1-x}Al_x$, and (c) $Li_{1-x}Zn_x$ systems with x = 0.05-0.50.

Supplementary Figure 3 provides additional compositional analysis complementing Figure 3, demonstrating the distinct protection mechanisms across the three systems after 20 ps simulations. $Li_{1-x}Mg_x$ systems show that Mg atoms actively participate in SEI formation even at low concentrations. In contrast, $Li_{1-x}Al_x$ and $Li_{1-x}Zn_x$ systems reveal surface segregation phenomena, where alloying elements concentrate at the anode-electrolyte interface rather than participating in SEI formation. Li-Mg systems demonstrate robust and uniform SEI formation, while Li-Al and Li-Zn systems exhibit unstable SEI similar to pure Li but with surface segregation. The suppression capability improves as alloy concentration increases across all systems.

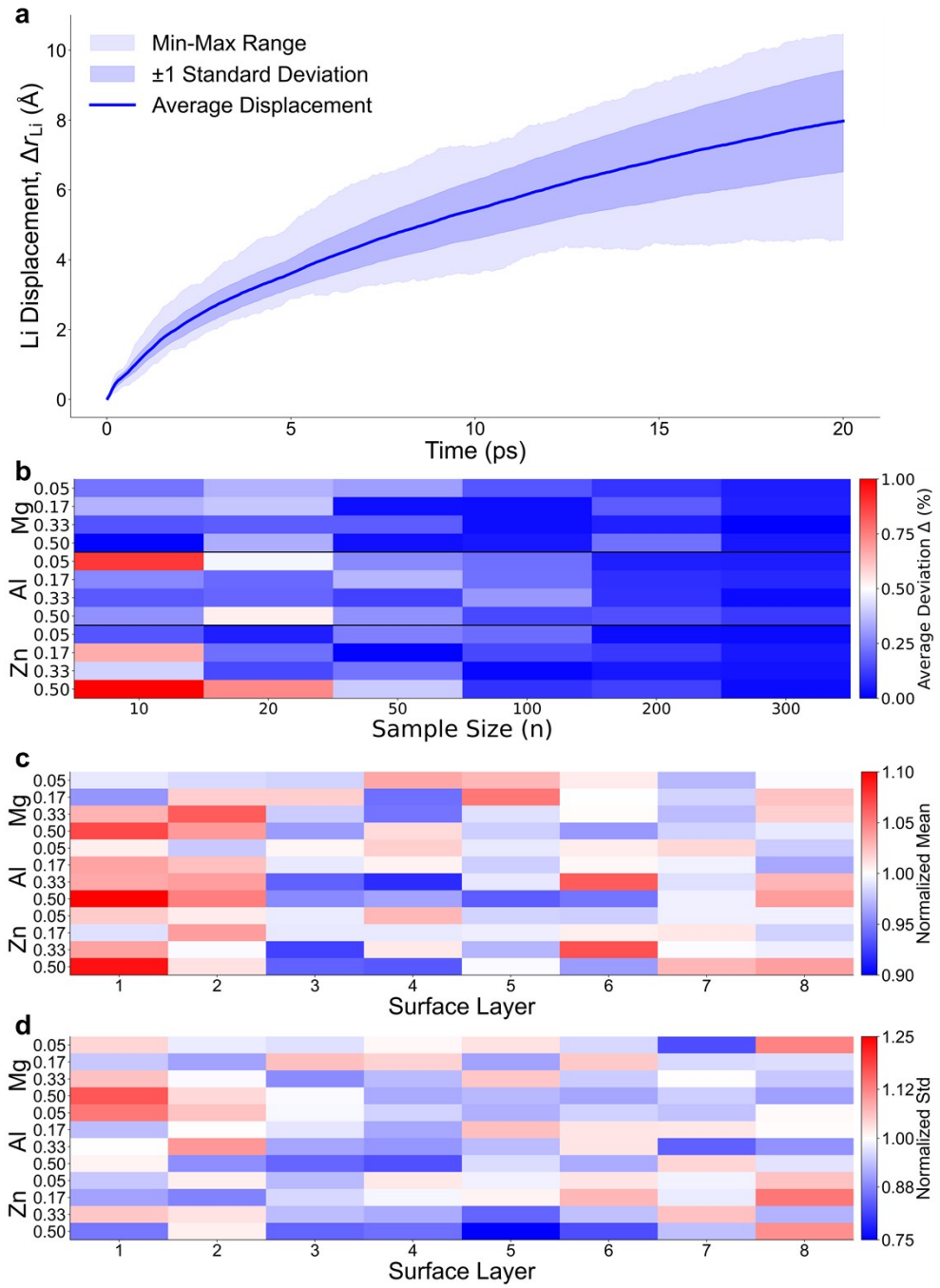

Supplementary Figure 4. Statistical analysis of Li displacement: (a) Time evolution in pure Li showing average (blue line), ±1 standard deviation (darker shade), and min-max range (lighter shade); (b) statistical convergence analysis heatmap displaying the average deviation (Δ) as a function of sample size (n) ranging from 10 to 300. (c-d) Layer-dependent variability across 8 atomic layers of $Li_{1-x}M_x$ alloys (M = Mg, Al, Zn; x = 0.05-0.50) at 20 ps showing (c) normalized mean and (d) normalized standard deviation relative to overall compositional averages. Red indicates higher values; blue indicates lower values.

1

Supplementary Figure 4 validates the statistical reliability of diverse interfacial structure simulations through comprehensive ensemble averaging analysis. Supplementary Figure 4a reveals the critical importance of this approach. It demonstrates the substantial variability in lithium migration behavior that occurs even under identical anode conditions. Since pure lithium anodes have identical composition across all layers, surface configurations are equivalent. However, the 50 different electrolyte molecular arrangements for each of the 8 surface configurations (totaling 400 interface structures) produce dramatically different Li displacement patterns despite having the same electrolyte concentration. The broad distribution spanning the min-max range and the substantial ±1 standard deviation bands highlight how electrolyte molecular positioning can cause variations reaching ±2 Å in final displacement values. This validates the necessity of multiple interface configuration simulations for reliable predictions.

To rigorously validate the sufficiency of our sampling size (400 configurations), we performed a statistical convergence analysis. Supplementary Figure 4b displays the average deviation (Δ) obtained by randomly sampling 100 independent subsets for each sample size (n) ranging from 10 to 300. The heatmap demonstrates that the deviation decreases systematically and saturates near zero for all compositions, confirming that our sampling is statistically converged.

Supplementary Figure 4c presents a heat map analysis showing that different anode surface layers exhibit distinct lithium migration behaviors at 20 ps, with ±10% variation from mean values across the eight surface configurations, demonstrating the significant influence of surface morphology on lithium displacement.

Supplementary Figure 4d illustrates the statistical reliability of our ensemble sampling approach (8 surface configurations × 50 electrolyte structures = 400 total configurations per composition) by analyzing the normalized standard deviation for each alloy composition at 20 ps. The analysis shows that most compositions achieve normalized standard deviations of 0.973 on average, demonstrating sufficient statistical sampling. However, higher-concentration Li-Al and Li-Zn systems (x = 0.50) show slightly lower values of 0.935 and 0.901.

This quantitative difference reflects fundamentally distinct protection mechanisms. Li-Al/Zn systems display large variability between different surface atomic configurations (±10%, Supplementary Fig. 4c), but low variability across different electrolyte configurations on the same surface (normalized std ~ 0.90). This indicates that surface atomic morphology is the dominant factor: once a stable Al/Zn segregation pattern forms at a given surface, it provides consistent physical protection largely independent of the dynamic electrolyte arrangement. In contrast, Li–Mg systems show relatively small variability between different surface atomic configurations, but large variability across electrolyte configurations on a given surface (normalized std ~ 0.98). This suggests that surface structure and electrolyte arrangement contribute comparably, consistent with the Mg co-migration mechanism in which dynamic interfacial chemistry plays a critical role.

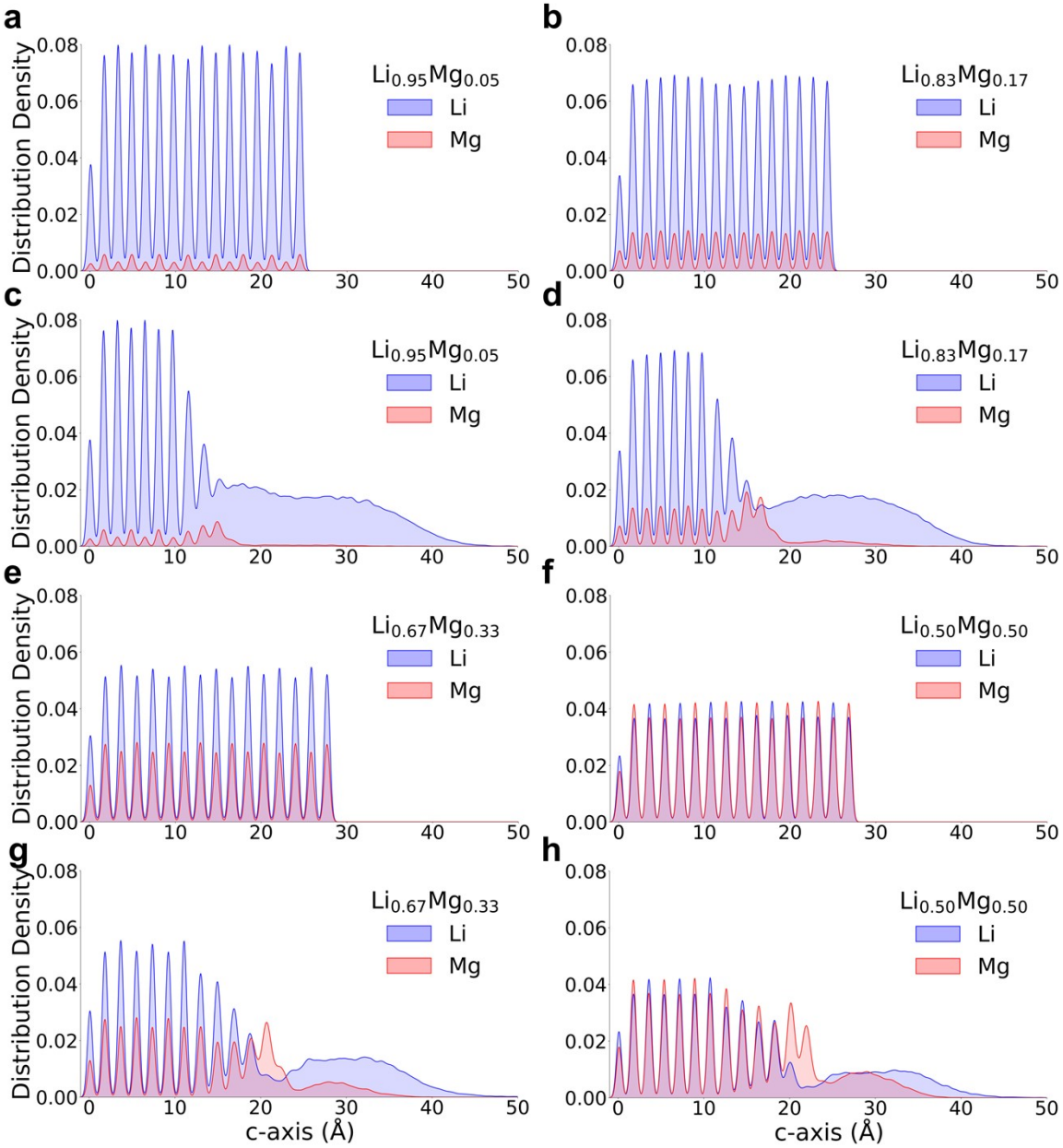

Supplementary Figure 5. Distribution density profiles of Li and Mg atoms along the c-axis in $Li_{1-x}Mg_x$ alloy anodes: comparison of elemental distributions at the initial state (0 ps; (a), (b), (e), (f)) and after 20 ps of simulation ((c), (d), (g), (h)).

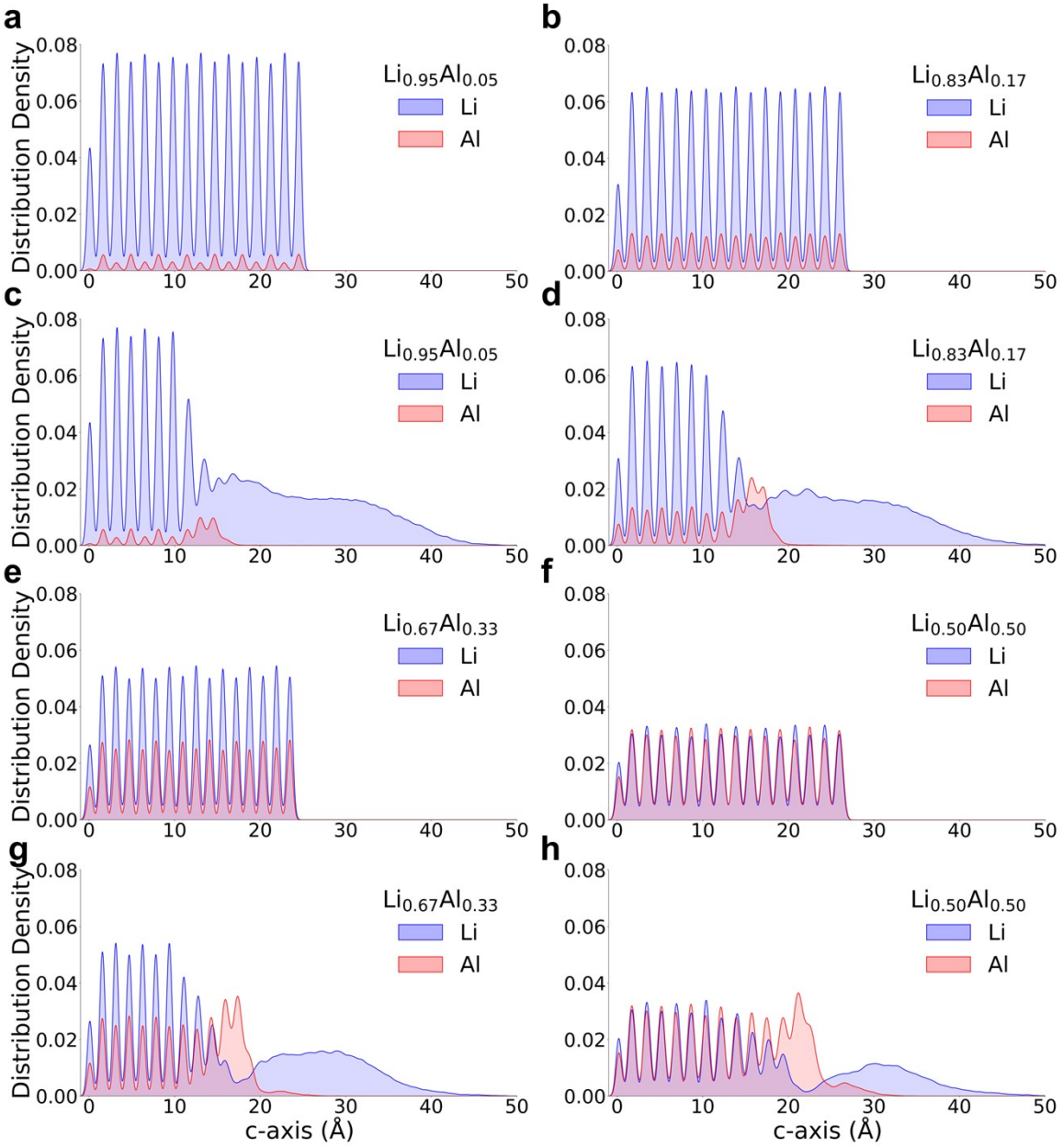

Supplementary Figure 6. Distribution density profiles of Li and Al atoms along the c-axis in $Li_{1-x}Al_x$ alloy anodes: comparison of elemental distributions at the initial state (0 ps; (a), (b), (e), (f)) and after 20 ps of simulation ((c), (d), (g), (h)).

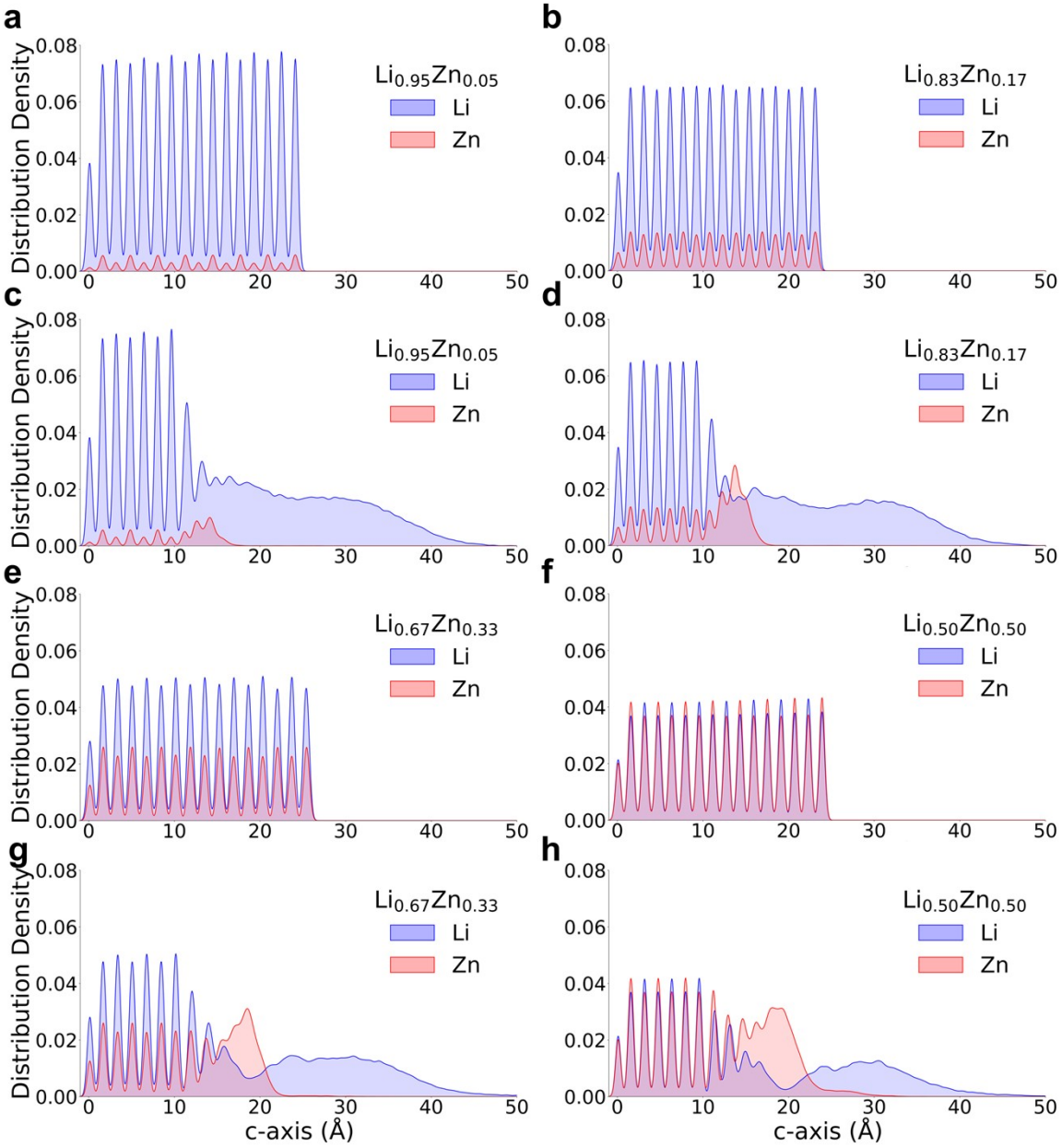

Supplementary Figure 7. Distribution density profiles of Li and Zn atoms along the c-axis in $Li_{1-x}Zn_x$ alloy anodes: comparison of elemental distributions at the initial state (0 ps; (a), (b), (e), (f)) and after 20 ps of simulation ((c), (d), (g), (h)).

Supplementary Figures 5-7 provide detailed breakdowns of Figure 5, presenting compositional analysis with enhanced granularity to facilitate comprehensive examination of distinct reorganization behaviors across the three alloy systems during interfacial exposure to electrolyte environments. The initial uniform atomic arrangements undergo systematic transformations that depend strongly on both alloy type and concentration. Li-Mg systems demonstrate cooperative migration behavior, where Mg atoms migrate together with Li atoms toward the interface, creating overlapping distribution profiles. This co-migration becomes increasingly pronounced at higher Mg concentrations, enabling enhanced interfacial protection through coordinated behavior. In contrast, Li-Al and Li-Zn systems exhibit surface segregation, where alloying elements accumulate at the anode-electrolyte interface while Li atoms migrate into the electrolyte. Surface segregation intensifies with increasing Al and Zn concentrations, creating distinct interfacial barriers.

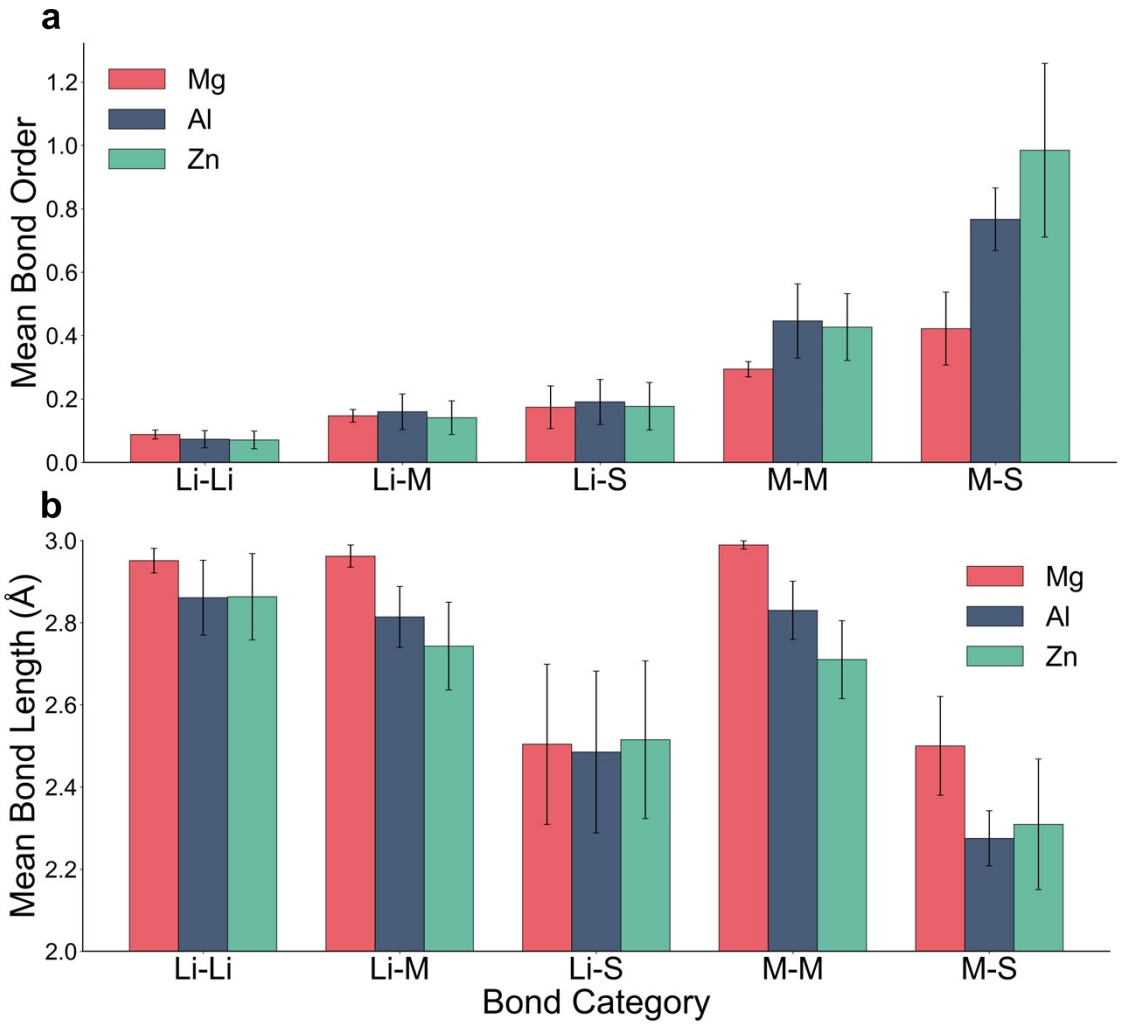

Supplementary Figure 8. Statistical analysis of atomic bonding in Li-M (M = Mg, Al, Zn) alloy anodes and SEI layers: (a) Mean bond order and (b) Mean bond length for pairs with distances ≤ 3.0 Å, categorized by bond type (alloy anode: Li-Li, Li-M, M-M; SEI: Li-S, M-S)

Supplementary Figure 8 quantifies the bonding characteristics within alloy anodes and their corresponding SEI layers based on bonds ≤ 3.0 Å identified in Figure 6, revealing that strong Zn-Zn and Al-Al metallic bonding promotes surface segregation behavior, while moderate Mg-S bonds enable cooperative migration and effective SEI formation. Supplementary Figure 8a demonstrates that M-S bonds exhibit the highest bond orders: Zn-S (1.0) > Al-S (0.77) > Mg-S (0.43). Despite their stronger bonding, Zn-S and Al-S interactions contribute minimally to

SEI formation due to surface segregation. The bond order progression Li-Li < Li-M < M-M (0.07-0.09 < 0.13-0.17 < 0.29-0.45) indicates enhanced mechanical stability in alloy anodes, where the stronger metallic bonding provided by alloying elements reinforces the structural integrity compared to pure lithium systems. Supplementary Figure 8b reveals that M-S bonds consistently exhibit the shortest bond lengths across all systems, demonstrating the general trend that stronger bonding interactions correspond to shorter bond lengths.

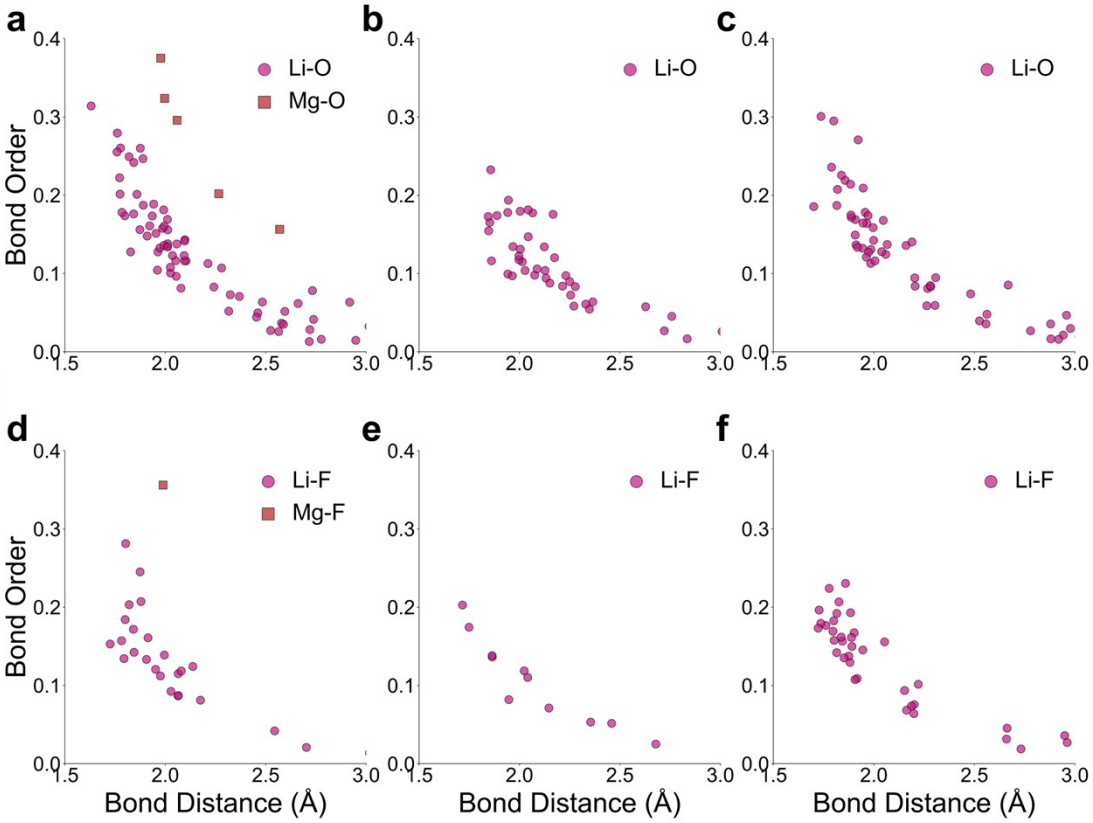

Supplementary Figure 9. DDEC6 bond order analysis for electrolyte-derived SEI components: (a-c) metal–oxygen bonding and (d-f) metal-fluorine bonding for $Li_{1-x}Mg_x$, $Li_{1-x}Al_x$ and $Li_{1-x}Zn_x$ alloy systems, respectively.

Supplementary Fig. 9 presents bond order analysis for metal-oxygen and metal-fluorine interactions at the anode-electrolyte interface, revealing the participation of electrolyte-derived

species in SEI formation across different alloy systems. The oxygen atoms originate from both DOL solvent and LiTFSI salt molecules, while fluorine atoms exclusively come from LiTFSI decomposition. Our analysis confirms that DOL molecules remain largely intact during the simulation period, whereas LiTFSI undergoes decomposition at the anode-electrolyte interface, contributing both oxygen- and fluorine-containing species to the SEI layer.

The metal-oxygen bonding analysis (Supplementary Fig. 9a-c) shows that Li-O bonds (0.13 ± 0.07) are present across all three alloy systems, indicating consistent interaction between lithium and oxygen-containing species from the electrolyte. In the Li-Mg system (Supplementary Fig. 9a), additional Mg-O bonds (0.27 ± 0.09) are observed with notably higher bond orders than Li-O interactions. Although Mg-O bonds are less abundant than Li-O bonds, their stronger bonding character suggests meaningful participation in SEI formation. In contrast, Li-Al and Li-Zn systems (Supplementary Fig. 9b,c) show virtually no Al-O or Zn-O bonding, indicating that aluminum and zinc atoms do not form significant chemical interactions with oxygen species.

Similarly, the metal-fluorine bonding analysis (Supplementary Fig. 9d-f) demonstrates that Li-F bonds (0.14 ± 0.06) constitute the majority of metal-fluorine interactions across all systems. The Li-Mg system shows limited Mg-F bonding (0.35) with bond orders approximately 2.5 times higher than Li-F bonds, while Al-F and Zn-F bonds are essentially absent in their respective systems.

Compared to metal-sulfur bonding (Fig. 6: Li-S 0.18 ± 0.07, Mg-S 0.42 ± 0.12, Al-S 0.77 ± 0.10, Zn-S 0.99 ± 0.27), metal-oxygen and metal-fluorine bonds show comparable or moderately lower bond orders for lithium interactions, while Mg-O (0.27 ± 0.09) and Mg-F (0.35) bonds are substantially weaker than Mg-S bonds (0.42 ± 0.12). Nevertheless, the

presence of Mg-O bonds in the Li-Mg system confirms that magnesium participates in forming multi-component SEI layers.

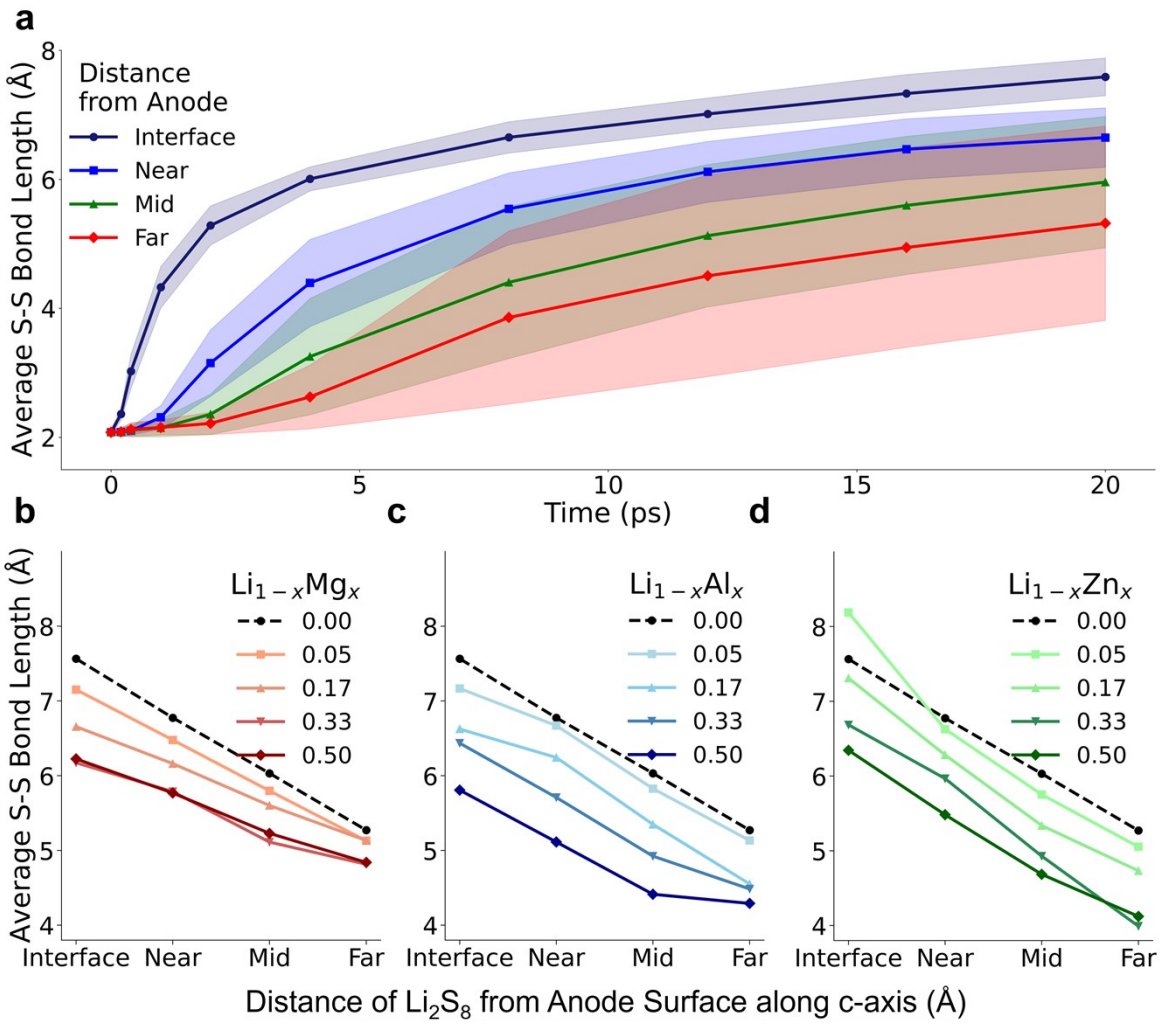

Supplementary Figure 10. Distance-dependent S-S bond evolution analysis of Li_2S_8: (a) time-dependent bond length changes of Li_2S_8 at different distances from pure Li anode surface; (b-d) bond lengths of Li_2S_8 at different distances from anode surface after 20 ps for $Li_{1-x}M_x$ alloys (M = Mg, Al, Zn).

Supplementary Figure 10 examines the spatial and temporal evolution of S-S bond lengths within Li_2S_8 molecules as a function of distance from different anode surfaces, providing insights into polysulfide stability and degradation mechanisms. The spatial analysis divides the electrolyte region into four zones: interface (0-25%), near (25-50%), mid (50-75%), and far (75-100%) from the anode surface. Supplementary Figure 10a shows that S-S bonds in Li_2S_8 undergo progressive elongation over time when exposed to pure lithium anode surfaces, with the most pronounced changes occurring at the interface region. The increases in bond length

follow a clear spatial gradient: interface > near > mid > far, indicating that proximity to the anode surface accelerates polysulfide decomposition. Supplementary Figure 10b-d reveal distinct compositional effects on S-S bond stability across the three alloy systems after 20 ps simulation.

REFERENCE

[1] D. B. Miracle and O. N. Senkov, *Acta Mater.*, 2017, **122**, 448. https://doi.org/10.1016/j.actamat.2016.08.081

[2] W. Nie, H. Cheng, Q. Sun, S. Liang, X. Lu, B. Lu and J. Zhou, *Small Methods*, 2024, **8**, 2201572. https://doi.org/10.1002/smtd.202201572

[3] M. Wang, F. Zhang, C. S. Lee and Y. Tang, *Adv. Energy Mater.*, 2017, **7**, 1700536. https://doi.org/10.1002/aenm.201700536

[4] M. Siniscalchi, J. Liu, J. S. Gibson, S. J. Turrell, J. Aspinall, R. S. Weatherup, M. Pasta, S. C. Speller and C. R. Grovenor, *ACS Energy Lett.*, 2022, **7**, 3593. https://doi.org/10.1021/acsenergylett.2c01793

[5] S. Yin, N. Wang, H. Han, Z. Liu, G. Zhang and R. Guan, *Metals*, 2024, **14**, 1202. https://doi.org/10.3390/met14111202